Foldover ferromagnetic resonance and damping in permalloy microstrips

Y. S. Gui, A. Wirthmann, and C.-M. Hu
Department of Physics and Astronomy, University of Manitoba, Winnipeg, Canada R3T 2N2
(Received 25 August 2009; revised manuscript received 23 October 2009; published 23 November 2009)

We have investigated the foldover ferromagnetic resonance in ferromagnetic permalloy (Py) microstrips by microwave photovoltage and photoresistance techniques. We have found that the linewidth of the nonlinear ferromagnetic resonance is strongly dependent on the precession angle of magnetization. Therefore, we have revised the Anderson-Suhl instability, which enables us to quantitatively describe the foldover effect in Py microstrips. The calculation from this proposed model shows excellent agreement with experimental data.

DOI: 10.1103/PhysRevB.80.184422 PACS number(s): 76.50.+g, 42.65.−k, 75.40.Gb

I. INTRODUCTION

One of the technological problems in current magnetic storage devices is that a high static magnetic field is needed to reverse the magnetization, which becomes more and more difficult to achieve because of the increased magnetic anisotropy for both the high density and the high stability of devices.[1] An alternative route is to use nonlinear effects, for example, microwave (MW)-assisted switching of magnetization proposed by Thirion *et al.*,[2] which has demonstrated its feasibility by several works.[3–6] On the other hand, the recording process requires fast magnetization reversal. Traditionally, the rate of remagnetization is regarded to be dominated by the Gilbert damping term[7] and the intrinsic Gilbert damping constant α stands for unspecified dissipative phenomena that can only be determined experimentally, normally by the linewidth ΔH_0 of ferromagnetic resonance (FMR) according to

$$\Delta H_0 = \Delta H_i + \alpha\omega/\gamma, \tag{1}$$

where ΔH_i is the FMR line-shape broadening due to the sample imperfections, ω is the MW frequency, and γ is the gyromagnetic ratio. There is no doubt about the validity of Eq. (1) for sufficiently small procession angles. Recently, Dobin and Victora[8] proposed an intrinsic mechanism of nonlinear ferromagnetic relaxation in thin metallic films based on the Suhl instability.[9] This four-magnon scattering dominates the competing linear mechanism and implies the inadequacy of Eq. (1) in nonlinear regime. Tiberkevich and Slavin[10] proposed another nonlinear model of magnetic dissipation, wherein the standard Gilbert model is generalized by regarding α to be a function of $(\partial\mathbf{M}/\partial t)^2$ in the framework of the phenomenological approach. This model has illustrated its application to describe the magnetic dissipation in a magnetic nanopillar,[10] which is so small that nonlinear magnon-magnon interactions are prohibited because spatial variation of the spin orientation would involve too much exchange energy.

Another effect linked to magnetization switching is the large-angle precession, which results in a frequency shift of FMR with its precession angle. Physicists have well known that the isochronism of a harmonic oscillator, such as a pendulum, is broken and results to bistability and foldover effects in the nonlinear regime when taking the nonlinear restoring force into account.[11] A seemingly different way was used to predicate the instability in the motion of FMR at higher MW power levels by Anderson and Suhl[12] in 1955. However, from the viewpoint of physics, they are the same; both of them are due to the amplitude-dependent eigenfrequency of the system. In 1958 Weiss[13] first described the anharmonic FMR response to explain the sideband oscillations produced in an yttrium iron garnet (YIG) disk. In the following half century, a number of authors[14–26] have worked on foldover FMR in ferrites. However, as pointed out by Seagle *et al.*,[20] no clear evidence for the existence of such an intrinsic foldover FMR predicted by Anderson and Suhl[12] has been produced. The magnetocrystalline anisotropy, sample heating, and high Q cavity interaction are believed to complicate earlier works.[25] Even when carefully designing the experiment to avoid these problems, Fetisov *et al.*[25] found a large difference between the predictions from the Anderson-Suhl model and the YIG film data; therefore, they doubted the inadequacy of this classic model. In addition, Chen *et al.*[24] showed that this classic model might explain the MW power dependence of one jump in the YIG foldover data by forcing the linewidth to be linearly proportional to MW field h; however, it failed to explain another jump, which is insensitive to the linewidth.

Since there is a lack of techniques to precisely detect the magnetic dissipation in nonlinear regime, there are two open questions: one is determining a phenomenological expression for damping (linewidth) at nonlinear magnetic dissipation, and another is how to revise the Anderson-Suhl model in the framework of a phenomenological approach. In this paper we will answer these questions in detail.

In order to study the FMR damping in the nonlinear regime and search for the Anderson-Suhl intrinsic foldover effect, we use MW photovoltage (PV) and photoresistance (PR) techniques[27–30] to detect FMR response for permalloy (Py) ($Ni_{80}Fe_{20}$, Py) microstrips deposited on a semi-insulating GaAs substrate. The simplest case which shows the physical origin of the nonlinear effect occurs in a thin film under a perpendicular applied static magnetic field, where the magnetization circularly precesses about the surface normal. Mathematically this precession can be simplified as a motion with one degree of freedom by using the concept of cone angle. We have successfully observed the FMR foldover effect in a metallic ferromagnetic strip from both the PV and PR spectra. Traditionally, a ferromagnetic metal is not a good candidate for the investigation of nonlinear effects since its linewidth is at least one order of magni-

tude wider than that in ferrite such as YIG. However, the thermal properties of the Py microstrip under the MW illumination[30] make it possible to observe a pure intrinsic foldover effect, since the temperature increases only a few kelvins corresponding to less than a 0.5 mT decrease in the saturation magnetization for a few 100 mW MW output power in our samples. In contrast, the saturation magnetization in YIG may shift more than 10 mT at high MW power levels.[26]

Phenomenologically, as discussed in Ref. 31 Eq. (1) has been generalized at nonlinear regime as

$$\Delta H = \Delta H_i + \alpha\omega/\gamma + \beta M_0 \theta^2, \tag{2}$$

where β is a dimensionless constant dependent on frequency, M_0 is the saturation magnetization, and θ is the cone angle of precession. In this paper, we establish a connection between this model and the experimental observation. By using Eq. (2) we revised the Anderson-Suhl model. This model can quantitatively model the experimental results. The goal of this paper is to provide a consistent view for describing the nonlinear FMR foldover response. The experimental observation is compared with the theoretical results in detail. The paper is organized in the following way. In Sec. II, a theoretical model has been made to describe the nonlinear FMR response based on a nonlinear oscillator. Section II A discusses a nonlinear oscillator including both the nonlinear restoring forces and nonlinear friction forces. A mathematical process has been provided to solve this kind of problem in general. Sections II B and II C extend this method to find the monofrequency in nonlinear spin dynamic systems with several degrees of freedom, with and without the nonlinear damping term, respectively. This enables us to directly characterize the damping property from the experimental observation.

Sample structure and experimental setup are discussed in Sec. III and the experimental results are presented in Sec. IV. We focus in particular on the jumps in the FMR foldover response and their dependence on the MW power (P) and MW field (h), which can prove the inadequacy of Eq. (1) in nonlinear regime. In Sec. Vconclusions are presented.

II. THEORY OF NONLINEAR FMR

A. General picture of nonlinear oscillations

To highlight the general feature of the complicated nonlinear spin dynamics, we first study the classical nonlinear oscillator with a mass m driven by an external force $f\sin(\omega t)$ with one degree of freedom, which can be solved from the equation of motion

$$\ddot{x} + 2\lambda\dot{x} + \omega_0^2 x = (f/m)\sin(\omega t) + g(x,\dot{x}). \tag{3}$$

The left-hand side of Eq. (3) includes the linear restoring force with the frequency ω_0 for the free oscillation of the system in the absence of friction, and the linear frictional force with damping coefficient λ. The right-hand side includes the external force f, with a simple periodic function of time, and $g(x,\dot{x})$, the nonlinear restoring force and friction force. Complete analytical solutions are not always available for Eq. (3) for a nonlinear system, where $g(x,\dot{x}) \neq 0$, and sometimes a special treatment[32,33] is needed to deduce quantitative results. The asymptotic methods developed by Bogoliubov and Mitropolsky[33] can be used to solve this problem, which provide a quite simple expression of the amplitude a for an oscillator near the resonance as

$$a^2 = \frac{f^2/m^2}{(\omega^2 - \omega_e^2)^2 + 4\omega_0^2\lambda_e^2} \approx \frac{f^2/4\omega_0^2 m^2}{(\omega - \omega_e)^2 + \lambda_e^2}, \tag{4}$$

where

$$\omega_e^2 = \omega_0^2 - \frac{1}{a\pi}\int_0^{2\pi} g(a\cos\psi, -a\omega\sin\psi)\cos\psi d\psi, \tag{5a}$$

$$\lambda_e = \frac{\omega}{\omega_0}\lambda + \frac{1}{2a\pi\omega_0}\int_0^{2\pi} g(a\cos\psi, -a\omega\sin\psi)\sin\psi d\psi. \tag{5b}$$

The expression of a^2 in Eq. (4) is very similar to a Lorentz line-shape resonator in the linear range. However, it should be noticed that the eigenfrequency (ω_e) and damping (λ_e) in Eq. (4) are in general functions of the amplitude a, which results in a complicated nonlinear response; for example, a nonlinear restoring force $g(x,\dot{x}) = -\eta x^3$ in a pendulum results to a foldover effect as detailed discussed in Refs. 11 and 34. The focus of this paper is to investigate the previously rarely studied effects of a nonlinear friction force such as a $-\lambda'\dot{x}^3$ ($\lambda' > 0$) term in $g(x,\dot{x})$. In this case the damping term in Eq. (4) is replaced with $\lambda_e = \lambda + 3a^2\omega_0^2\lambda'/8$ according to Eq. (5b). Due to this additional amplitude-dependent damping, several effects appear. One pronounced effect is that the foldover effect will not appear in the range where $|\eta| < \sqrt{3}\lambda'\omega_0^3$ no matter how strong an f is applied. Its mathematical proof will be provided in Sec. II C in detail. Another effect is that the amplitude of the motion decays as

$$a(t) = a_0\sqrt{\frac{\lambda}{\frac{3}{8}\omega_0^2 a_0^2\lambda'(e^{2\lambda t} - 1) + \lambda e^{2\lambda t}}}, \tag{6}$$

according to $da/dt = -\lambda_e a$ if removing the force at $t=0$, where a_0 is the amplitude at $t=0$. It is found that a decays much faster than the exponential decay $a(t) = a_0 e^{-\lambda t}$ for $\lambda' = 0$.

B. Nonlinear FMR with linear Gilbert damping

Ferromagnetic resonance presents an excellent model for studying nonlinear dynamics. The precessional motion of a magnetic moment is described by the torque equation with a dissipative term proportional to the generalized velocity, $\partial\mathbf{M}/\partial t$. This gives the Landau-Lifshitz-Gilbert (LLG) equation of motion

$$\frac{\partial\mathbf{M}}{\partial t} = -\gamma\mathbf{M}\times\mathbf{H}_{eff} + \frac{\alpha}{M_0}\mathbf{M}\times\frac{\partial\mathbf{M}}{\partial t}, \tag{7}$$

where $\mathbf{H}_{eff}$ is the effective magnetic field. For the case of FMR and neglecting the exchange interaction, the LLG

equation describes a monofrequency oscillation in a spin system with several degrees of freedom. For a perpendicular static field H (along the surface normal z direction), $\mathbf{H}_{eff}=(h\cos[\omega t],h\sin[\omega t],H-M_z)$ and $\mathbf{M}=(m_x,m_y,M_z)$ are used to determine the dynamic response under a circular excitation, where the in-plane microwave field h is $h=S\sqrt{P}$, where P is the microwave output power and S is a coupling parameter dependent on the sample design and ω. It is found that in this case the magnetization circularly precesses along the z direction with a cone angle according to

$$\theta^2=\frac{(1-\theta^2/2)^2h^2}{(H-M_0+M_0\theta^2/2-\omega/\gamma)^2+(\alpha\omega/\gamma)^2(1-\theta^2/2)^2}. \tag{8}$$

Neglecting the higher-order $h^2\theta^2$ and $\alpha^2\theta^2$ terms, Eq. (8) becomes the well-known form of cone angle in the nonlinear regime,

$$\theta^2=\frac{h^2}{(H-H_0+M_0\theta^2/2)^2+\Delta H_0^2}, \tag{9}$$

where $H_0=\omega/\gamma+M_0$ is the resonance position at $h\to 0$, and $\Delta H_0=\alpha\omega/\gamma+\Delta H_i$. It should be noted that in general magnetization elliptically precesses for an arbitrary $\mathbf{H}$ ($\dot{M}_z\neq 0$) and the LLG equation cannot be simplified by the concept of cone angle. However, the asymptotic methods are available to solve the LLG equation in any configuration.[33]

Mathematically, the nonlinear FMR described in Eq. (9) is similar to the solution of a pendulum according to Eq. (4) with a nonlinear restoring force term $g(x,\dot{x})=-\eta x^3$. When h is stronger than a critical field h_{th}, FMR response shows the discontinuity of θ at $d\theta/dH=\pm\infty$ indicated by the arrows in Fig. 1(c).

Using a similar method as done for the pendulum,[11] we can quantitatively determine the jump positions in FMR. Differentiating Eq. (9) with respect to H, we have

$$\frac{d\theta}{dH}=-\frac{\theta\left(H-H_0+\frac{1}{2}M_0\theta^2\right)}{\left(H-H_0+\frac{1}{2}M_0\theta^2\right)\left(H-H_0+\frac{3}{2}M_0\theta^2\right)+\Delta H_0^2}. \tag{10}$$

Therefore the up and down jumps can be determined from the quadratic equation of θ^2,

$$\left(H-H_0+\tfrac{1}{2}M_0\theta^2\right)\left(H-H_0+\tfrac{3}{2}M_0\theta^2\right)+\Delta H_0^2=0, \tag{11}$$

which has two real roots, namely, θ_{up} and θ_{down} for $h\geq h_{th}$. H_{up} and H_{down} indicated by the arrows in Fig. 1(c) represent the jump-up and- down points in the response curve, respectively. The threshold field corresponds to $\theta_{up}=\theta_{down}$, then one can get $H_{up}=H_{down}=H_0-\sqrt{3}\Delta H_0$ and $\theta_{up}^2=\theta_{down}^2=4\sqrt{3}\Delta H_0/3M_0$. Substituting them into Eq. (9), the critical field is $h_{th}^2=16\sqrt{3}\Delta H_0^3/9M_0$, which is same as the previous value deduced by Anderson and Suhl.[12]

Experimentally, H_R, H_{up}, and H_{down}, which correspond to $d\theta/dH=0$, $d\theta/dH=+\infty$, and $d\theta/dH=-\infty$, respectively, are of the most interest. H_R is the maximum of the response curves

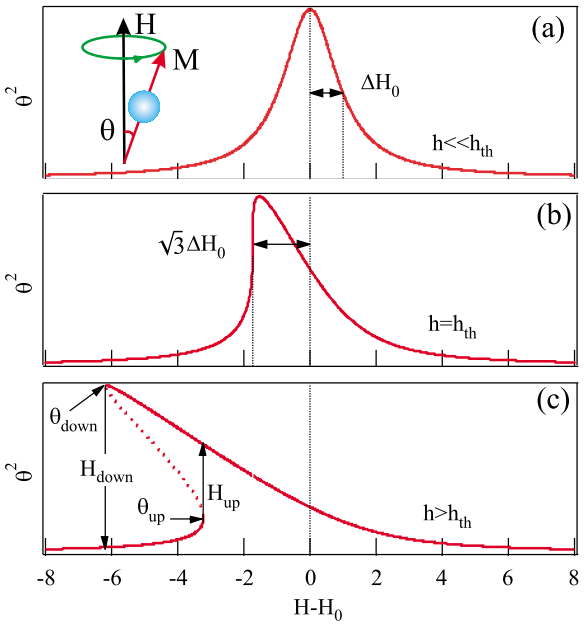

FIG. 1. (Color online) The calculated θ^2, as a function of $H-H_0$ for a FMR at (a) $h=0.01h_{th}$, (b) $h=h_{th}$, and (c) $h_{rf}=2h_{th}$, respectively. For simplest dimensionless parameters $M_0=1000$, $H_0=1100$, and $\Delta H_0=1$ are used for calculation. The dotted lines represent $H-H_0=0$, $H-H_0=\Delta H_0$, and $H-H_0=-\sqrt{3}\Delta H_0$, respectively.

and has a simple form according to Eqs. (10) and (9),

$$H_R=H_0-\frac{1}{2}\frac{h^2}{\Delta H_0^2}M_0. \tag{12}$$

H_{up} and H_{down} can be solved as functions of h and have no analytical solution in general. We can simplify the solution of Eq. (11) as $\theta_{up}^2\approx -2(H_{up}-H_0)/3M_0$ and $\theta_{down}^2\approx -2(H_{down}-H_0)/M_0$, for $h\gg h_{th}$, and then get

$$H_{up}\approx H_0-\frac{3}{2}h^{2/3}M_0^{1/3}\quad \text{at}\quad \theta_{up}=(h/M_0)^{1/3},$$

$$H_{down}\approx H_0-\frac{1}{2}\frac{h^2}{\Delta H_0^2}M_0\quad \text{at}\quad \theta_{down}=h/\Delta H_0. \tag{13}$$

The available range of Eqs. (13) can be verified by the comparison between the analytical results (lines) and the numerical calculation (symbols). As shown in Fig. 2 they are in good agreement for H_{down} in the whole range and for H_{up} at $h>2h_{th}$. Therefore, in the linear damping model $H_{down}\propto h^2(P)$ and $H_{up}\propto h^{2/3}(P^{1/3})$ have a different dependence of the microwave field (power). Meanwhile, H_{down} is inversely proportional to ΔH_0^2 and H_{up} is independent on ΔH_0.

C. Nonlinear FMR with nonlinear damping

For sufficiently small precession angles the standard linear damping has already shown its success for the last half century. However, Eq. (1) cannot explain the unique feature of nonlinear FMR as discussed in Ref. 31 and a nonlinear damping term as shown in Eq. (2) has to be taken into account. At this moment, we do not know the origin of the β

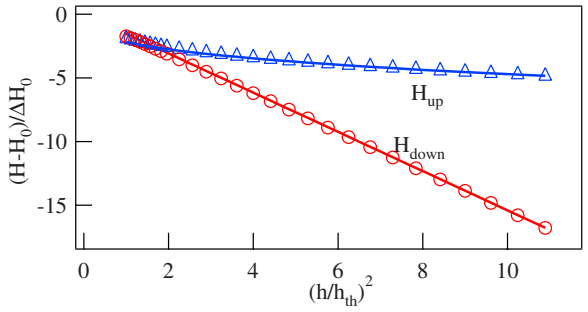

FIG. 2. (Color online) H_{up} and H_{down} as functions of h calculated from the analytical equation (13) (lines) in comparison with the numerical calculation (symbols) from Eq. (9). Notice that the foldover effect does not exist at $h<h_{th}$.

term since we cannot directly deduce it from the standard linear LLG equation for FMR(k=0). The standard linear LLG equation may result in a θ^2-dependent damping term as shown in Eq. (8); however, this additional damping term decreases with θ^2 and furthermore it cannot dominate the $\alpha\omega/\gamma$ term, which is in contrast to our experimental observation. Mathematically, a similar damping term proportional to a^2 appears if a nonlinear friction force $-\lambda' \dot{x}^3$ is taken into account in nonlinear oscillators as discussed in Sec. II A. If we introduce a higher-order friction force, the higher-order damping term (only with even orders of a) will appear. It is possible that the damping of FMR also has a similar form to

$$\Delta H = \Delta H_0 + \beta M_0 \theta^2 + \beta' M_0 \theta^4 + \cdots . \tag{14}$$

In this paper, we only deal with the nonlinear FMR response to θ^2 order for both the eigenfrequency and damping, which has demonstrated its precision in modeling experimental results. In this case, the cone angle in Eq. (9) can be generalized in the nonlinear regime as

$$\theta^2 = \frac{h^2}{\left(H - H_0 + \frac{1}{2}M_0\theta^2\right)^2 + (\Delta H_0 + \beta M_0 \theta^2)^2}. \tag{15}$$

Differentiating Eq. (15) and using the condition that $d\theta/dH = \pm\infty$ to determine the jump positions, we get

$$\left(H - H_0 + \tfrac{1}{2}M_0\theta^2\right)\left(H - H_0 + \tfrac{3}{2}M_0\theta^2\right) + (\Delta H_0 + \beta M_0\theta^2)(\Delta H_0 + 3\beta M_0\theta^2) = 0. \tag{16}$$

The two real roots of the quadratic equation (16) in θ^2 are doubly degenerate at

$$H - H_0 = \frac{-8\beta - \sqrt{3}(1+4\beta^2)}{1-12\beta^2}\Delta H_0 \tag{17}$$

and the corresponding root is

$$\theta^2 = \frac{4\sqrt{3}}{3(1-2\sqrt{3}\beta)}\frac{\Delta H_0}{M_0}. \tag{18}$$

Substitution of these values of $H-H_0$ and θ^2 into Eq. (15) gives the critical field h_{th},

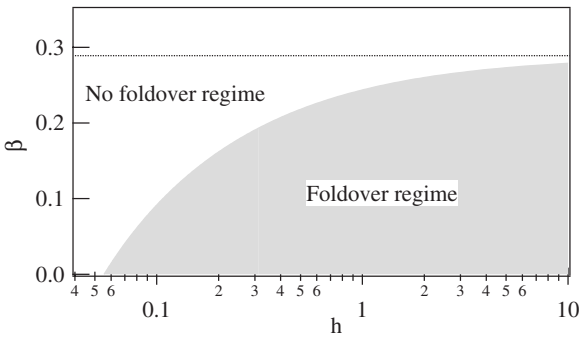

FIG. 3. Phase diagram of foldover FMR response by assuming M_0=1000, ΔH_0=1. The solid line represents $\beta=1/2\sqrt{3}$.

$$h_{th}^2 = \frac{16\sqrt{3}(1+4\beta^2)}{9(1-2\sqrt{3}\beta)^3}\frac{\Delta H_0^3}{M_0}. \tag{19}$$

The value of $h_{th}^2 = 16\sqrt{3}\Delta H^3/9M_0$ for $\beta=0$ is the same as that in the standard linear damping model. Taking nonlinear damping into account, the foldover response can be only observed at $12\beta^2<1$. Beyond this range, both θ and h_{th} have no real solution. Figure 3 shows the phase diagram of the FMR foldover response as a function of β and h. The foldover FMR response can be observed by increasing h to overcome the additional β damping term until to $\beta=1/2\sqrt{3}$. When $\beta \geq 1/2\sqrt{3}$, the foldover FMR cannot be excited no matter how strong an h is applied, because the shift of FMR cannot compensate the broadening of ΔH due to h. This is completely different from the result deduced from the standard linear damping model. At $\beta M_0\theta^2 \gg \Delta H_0$, where the damping is dominated by nonlinear damping term, analytical solutions for H_{up} and H_{down} can be found to be

$$H_{up} \approx H_0 - \frac{3}{2}M_0^{1/3}h^{2/3}\left[1 - \frac{1}{3}\beta^2 - \frac{7}{9}\beta^4 + O(\beta^6)\right], \tag{20}$$

$$H_{down} \approx H_0 - \frac{1}{2}\left(\frac{h}{\beta}\right)^{2/3} M_0^{1/3}[1 + 3\beta^2 + O(\beta^6)], \tag{21}$$

and correspond to different cone angles

$$\theta_{up}^2 \approx \frac{h^{2/3}}{M_0^{2/3}}\left(1 + 5\beta^2 + \frac{77}{9}\beta^4 + O(\beta^6)\right), \tag{22}$$

$$\theta_{down}^2 \approx \frac{h^{2/3}}{(\beta M_0)^{2/3}}[1 - 3\beta^2 + O(\beta^6)]. \tag{23}$$

Since the observation of the foldover FMR response is limited by the condition of $\beta<1/2\sqrt{3}$, H_{up} in Eq. (20) is only a few percent different from that in Eq. (13). However, $H_{down} \propto h^{2/3}$ shows a completely different dependence on h in comparison to $H_{down} \propto h^2$ in Eq. (13). This provides a direct way to verify the availability of standard linear damping in nonlinear range. It should be noted that $H_{down} \propto h^{2/3}$ holds true even for $\beta M_0\theta^2 < \Delta H_0$. In this case because of $|H_{down} - H_0 + \frac{1}{2}M_0\theta_{down}^2| \ll \Delta H_0$ in Eq. (15), H_{down} is found to be

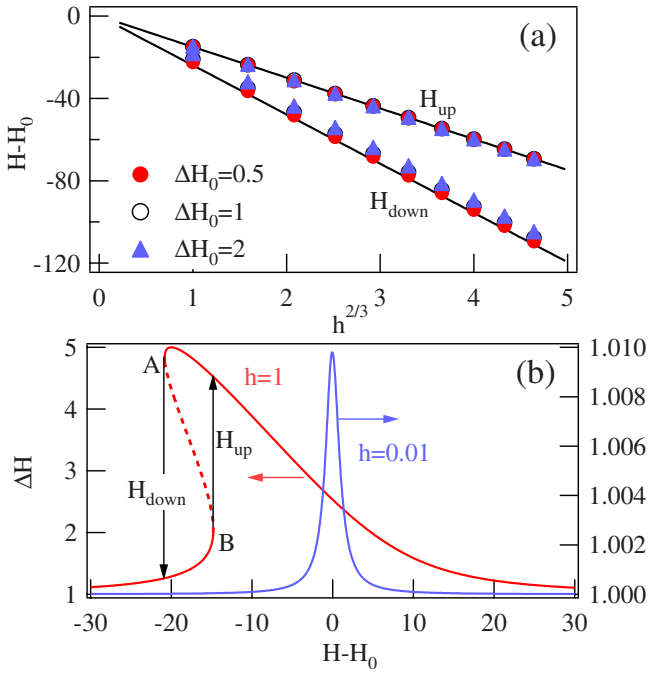

FIG. 4. (Color online) (a) Both H_{up} and H_{down} show a linear dependence on $h^{2/3}$ with $M_0=1000$ and nonlinear damping parameter $\beta=0.1$. Lines are calculated from Eqs. (20) and (21), respectively. Symbols are numerical results from Eq. (15) for several values of ΔH_0. (b) ΔH as a function of $H-H_0$ for $\beta=0.1$ and $\Delta H_0=1$ at $h=0.01$ and 1, respectively.

$$H_{down} \approx H_0 - \frac{1}{2}\left(\frac{h}{\beta}\right)^{2/3}(1+3\beta^2)M_0^{1/3} + \frac{1}{3\beta}\Delta H_0, \quad (24)$$

which is similar to Eq. (21) except for a shift term of $\Delta H_0/3\beta$. The numerical calculation of the foldover FMR according to Eq. (15) is also used to deduce H_{up} and H_{down} as shown by the symbols in Fig. 4(a) for several values of ΔH_0. As expected, H_{up} is found to be insensitive to ΔH_0 and is linearly dependent on $h^{2/3}$ as in Eq. (20). Meanwhile, H_{down} is also linearly dependent on $h^{2/3}$. Its slope is almost independent on ΔH_0 and it has a vertical shift on the order of ΔH_0, which is in agreement with Eq. (24).

Since the β term cannot be neglected, the time evolution of the damping has a sensitive dependence on initial conditions as that for motion. At low power excitation, ΔH is dominated by ΔH_0 by the standard linear damping as shown in Fig. 4(b). Increasing the MW power, the foldover effect of ΔH has also been found. The middle root indicated by the dashed line in Fig. 4(b) is unstable. A remarkable feature here is the existence of a range (between H_{up} and H_{down}) where two different ΔH's are possible. The value of ΔH in the response is dependent on the sweep direction of H. In the boundary of this area (A and B) ΔH is discontinuous and can only jump to another root.

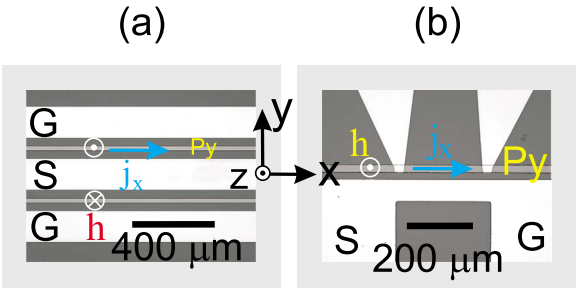

FIG. 5. (Color online) Top view optical micrograph of samples (a) A-3 and (b) B-1. The Py microstrip is deposited in the slot between the conductors of a ground-signal-ground (G-S-G) coplanar waveguide for sample A-3 and adjacent to the shorted end of G-S conductors for sample B-1. The directions of dynamic current j and dynamic magnetic field h are indicated by the arrows.

III. SAMPLE STRUCTURE AND MEASUREMENT SETUP

Several sets of spin dynamos are used in this work (Table I). The thickness and width of the Py microstrips are varied from 40 to 150 nm and from 2 to 40 μm, respectively. As shown in Fig. 5(a), sample set A from the first-generation spin dynamos[27] has two identical Py microstrips deposited in both slots between the conductors of a ground-signal-ground (G-S-G) coplanar waveguide (CPW). The dimension of such a CPW is designed to achieve a 50 Ω impedance. Sample set B shown in Fig. 5(b) is a modified version of sample A, where the Py microstrip is evaporated adjacent to the shorted end of G-S conductors. This structure increases the h field by increasing the MW current flowing in the shorted CPW. However, the direction of the h vector in such a lateral coupling structure, which will be verified in Sec. IV A, is close to the surface normal as that in sample A, and only have a weak in-plane h field contributing to the foldover effect. Therefore, samples A and B can be used to study the transition from linear to nonlinear FMR response. The x-y-z coordinate system used in this paper is plotted in the inset of Fig. 5, where the x axis is along the Py strip, the z axis is along

TABLE I. Summary of sample parameters.

Sample	Width (μm)	Thickness (nm)	$\mu_0 M_0$ (T)	$\gamma/2\pi$ (μ_0 GHz/T)	α	$\mu_0 \Delta H_i$ (mT)
A-3	20	137	1.03	28.6	0.0053	0.077
B-1	20	45	0.97	28.2	0.007	1.1
C-10	10	50	0.90	28.6	0.012	0.93
C-7	7	100	1.00	29.3	0.010	0.90
C-5	5	100	1.00	29.2	0.009	0.88

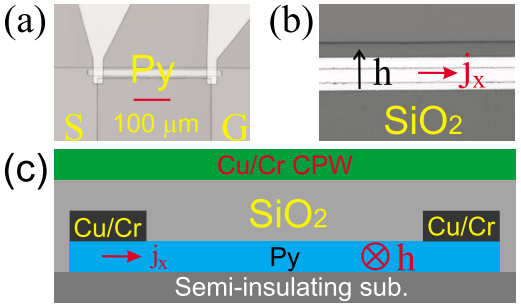

FIG. 6. (Color online) (a) Top view optical micrograph of sample C-5, where a Py microstrip with a size of $280\times5\times0.1$ μm^3 was embedded under the shorted conductor with a 10 μm width and a 200 nm SiO_2 between them was used as electrical insulating. (b) Enlarging the micrograph and (c) the schematic of the cross section the shorted end of CPW. The directions of dynamic current j and dynamic magnetic field h in the Py microstrip are indicated by arrows.

the surface normal, and the y axis is along the width direction of Py strip.

Sample set C as shown in Fig. 6 is the upgraded spin dynamo designed with vertical coupling architecture to achieve a desirable h vector in both strength and orientation. The Py microstrip is embedded under the shorted conductor of the S and G strips and is isolated from the CPW by a 200 nm SiO_2 layer to enable sensitive electrical detection of FMR. The sample is fabricated in the following steps: (1) thermal evaporating a 40–150 nm thickness Py film and lift-off to form a Py microstrip, (2) sputtering a 60/10 nm Cu/Cr layer for contacting leads, (3) sputtering a 200 nm SiO_2 layer for electrical insulating, and (4) sputtering a second 200/10 nm Cu/Cr layer for CPW and bonding patterns.

The parameters of Py microstrips differ slightly from sample to sample due to different fabrication processes and their geometry. The gyromagnetic ratio $\gamma/2\pi$ is $28.2\mu_0-29.3\mu_0$ GHz/T and the saturation magnetization $\mu_0 M_0$ is 0.90–1.05 T.

MW PV [Figs. 7(a) and 7(b)] and MW PR [Figs. 7(c) and 7(d)] were used to trace the FMR response in this paper. The MW PV presented in this paper is taken by slightly tilting the field direction away from the z axis toward the x axis with a very small angle of $0.01°-0.1°$, so that the x component of the magnetization M_x is nonvanishing because of PV $\propto M_x\langle m_x j_x\rangle$.[27] From the viewpoint of the signal/noise ratio, the PV technique has a big advantage since the PR technique, where an additional dc has to be applied, has a strong nonresonant background.[30] However, the PR technique can be used in an exactly perpendicular configuration and, furthermore, PR $\propto\langle m_x^2\rangle$ has a simpler relation to the magnetization procession.[29]

Under continuous-wave (CW) excitation the measurements results will show a splitting of the up- and down-sweep traces as shown in Figs. 7(b) and 7(d) at $h>h_{th}$. We also use the standard lock-in technique by 100% modulating the amplitude [amplitude modulation (AM)] of microwave power with a 8.33 kHz square wave. The lock-in technique significantly enhances the signal/noise ratio,[27,28] which enables us to detect a PV signal as weak as 10 nV. This can be found in Fig. 11(c). However, the modulation of MW power confuses initial conditions. As a result only one branch of the foldover FMR response appears in modulation measurements, as demonstrated in Figs. 7(a) and 7(c), no matter which direction of H sweeping. Similar results have been found by Fetisov *et al.*,[25] which show that the frequency sweep pulse data at fixed power reproduced the down-sweep CW results and at fixed frequency reproduced the increasing-power CW results.

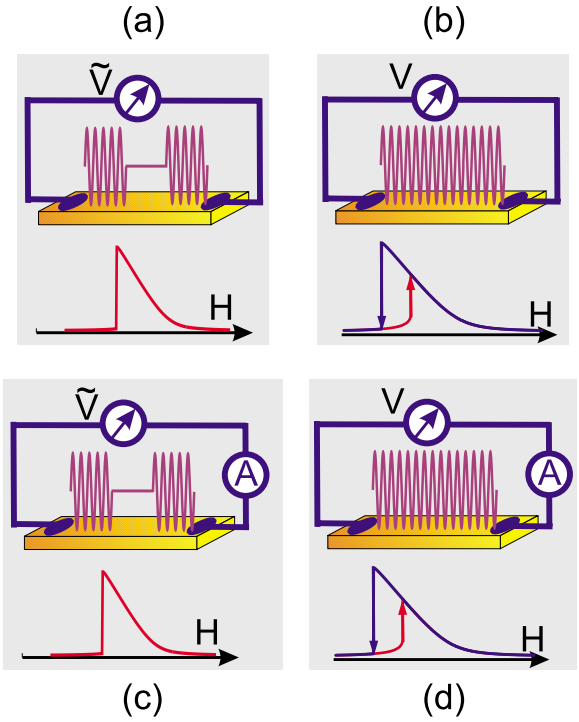

FIG. 7. (Color online) Schematic drawing of the Py microstrip, the measurement circuitry, and the typical response of FMR foldover effect. (a) and (b) are from the MW photovoltage (PV) technique and (c) and (d) are from the MW photoresistance (PR) technique. (b) and (d) are under continuous-wave (CW) excitation, which shows a splitting of up- and down-sweep traces, while (a) and (c) show an identical response for sweeps up and down when modulating the MW power.

IV. EXPERIMENTAL RESULTS AND DISCUSSION

A. h vector in a spin dynamo

Every sample has been calibrated first to detect the h vector in an in-plane H configuration.[29,35] Figure 8(a) shows a typical FMR resonance for a first-generation spin dynamo, sample B-1, at $\theta_H=135°$ at 15 dBm. The inset of Fig. 8(a) is the top view micrograph of sample B-1, which has a Py strip of 20 μm in width and 20 μm distance from the shorted end (50 μm in width) of the CPW. θ_H is the angle of the external applied in-plane H field with respect to the x axis. As discussed in detail in Refs. 29 and 35, the PV shows up as a resonant signal at FMR, with a line shape given by

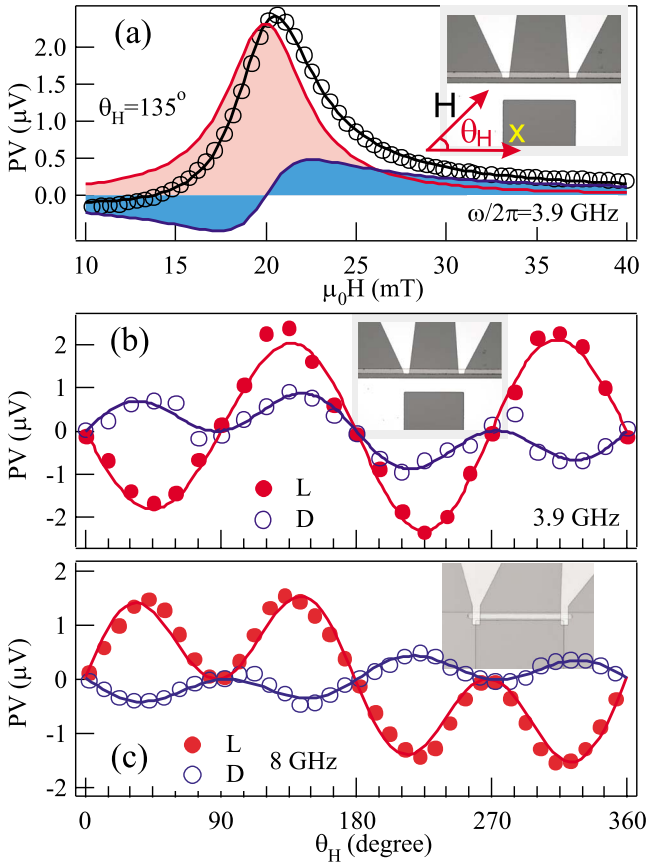

FIG. 8. (Color online) (a) Typical PV response of FMR at $\theta_H=135°$ for a first-generation spin dynamo (sample B-1), and its line shape is a superposition of a Lorentz- and a dispersive-type resonance. The MW frequency and the MW power are 3.9 GHz and 15 dBm, respectively. (b) The amplitudes (symbols) of Lorentz- (L) and dispersive- (D) type resonance as functions of θ_H and their fitting results (solid lines) for a first-generation spin dynamo (sample B-1). (c) The angle-dependent PV amplitude for a second-generation spin dynamo (sample C-7) at 8 GHz and 15 dBm for comparison.

$$\mathrm{PV} = L\frac{\Delta H^2}{(H-H_0)^2+\Delta H^2} + D\frac{\Delta H(H-H_0)}{(H-H_0)^2+\Delta H^2}. \quad (25)$$

The fitting results are $L=2.32$ μV, $D=0.96$ μV, $H_0=19.9$ mT, and $\Delta H=2.6$ mT. Furthermore, the amplitude of the Lorentz (L) and dispersive (D) line shapes are determined by[29,35]

$$L = -R_0R_AM_0j_x\sin(2\theta_H)\left[-A_{xx}h_y^i\cos(\theta_H)+A_{xx}h_x^i\sin(\theta_H)-A_{xy}h_z^r\right]/2, \quad (26a)$$

$$D = -R_0R_AM_0j_x\sin(2\theta_H)\left[A_{xx}h_y^r\cos(\theta_H)-A_{xx}h_x^r\sin(\theta_H)-A_{xy}h_z^i\right]/2, \quad (26b)$$

where $R_A=\Delta\rho/\rho M_0^2$ is the anisotropic magnetoresistance (AMR) coefficient with the resistivity ρ and the change in resistivity $\Delta\rho$ due to AMR effect and R_0 is resistance of the strip. The factor of 2 is caused by the time average. Note that the components h_x, h_y, and h_z represent complex numbers with real (r) and imaginary (i) parts, which account for their different phases with respect to the microwave current j_x. The coefficients A_{xx} and A_{xy} are given by

$$A_{xx}=\frac{H_0M_0+M_0^2}{\Delta H(2H_0+M_0)}, \quad A_{xy}=\frac{\omega M_0}{\gamma\Delta H(2H_0+M_0)}.$$

The dominated part of PV is L for both samples B-1 [Fig. 8(b)] and C-7 [Fig. 8(c)]. It shows a $\sin(2\theta_H)$ dependence and a $\sin(2\theta_H)\cos(\theta_H)$ dependence for two samples, respectively, which indicates that as expected the main part of h is h_z and h_y in the first- and second-generation spin dynamos, respectively.

Just for an example, we can further quantitatively estimate h vector in sample B-1. The value of j_xh is determined by fitting L and D [solid line in Fig. 8(b)] as functions of θ_H according to Eq. (26b), while other parameters in Eq. (26b), $\mu_0M_0=0.97$ T, $R_0=111.2$ Ω, and $\Delta\rho/\rho=0.0044$, are prior deduced from the AMR effect and FMR dispersion. For the purpose of separating j_x and h vector, the PR at $\theta_H=90°$ was measured and the FMR signal was found to be a Lorentz line shape with an amplitude of 12 $\mu\Omega$ at 15 dBm. After calculating $j_x\sim1.6$ mA from Eq. (19) in Ref. 29, we can obtain $\mu_0|h_x|\sim1.5$ μT, $\mu_0|h_y|\sim7$ μT, and $\mu_0|h_z|\sim90$ μT.

B. FMR dispersion and its standard linear Gilbert damping

In general the FMR is always accompanied by different kinds of spin waves, which may be the magnetostatic modes due to the dipole-dipole interaction, the standing spin waves due to the exchange interaction, or the dipole-exchange spin waves due to both the dipole-dipole interaction and exchange interaction. Sample A-3, with dimensions of 2.45 mm in length, 20 μm in width, and 137 nm in depth, shows the FMR and five magnetostatic forward volume modes in Fig. 9(a). The first observed magnetostatic forward volume mode and standing spin wave have distances of 6.7 and 78 mT away from FMR, respectively. The full spectra of standing spin waves and dipole-exchange modes have been discussed in detail in Ref. 28. Since spin-wave modes are very sensitive to the geometry configuration, the appearance of these modes indicates the excellent homogeneity of the sample.

The intrinsic Gilbert damping constant can be deduced from the linewidth of FMR at low power excitation, where μ_0h is about $0.01\Delta H$. The value of the Anderson-Suhl threshold μ_0h_{th} was estimated to be about 17 μT from Eq. (19) at 2.2 GHz by using the experimental value of $\mu_0\Delta H_0=0.45$ mT and assuming $\beta=0$. It is much higher than the value of $\mu_0h\sim4.5$ μT used in the experiment [solid lines in Fig. 9(b)]. Two Py microstrips show an identical effect in Fig. 9(c) and the dispersion can be excellently modeled by $\omega=\gamma(H-M_0)$ with $\gamma/2\pi=(28.57\pm0.04)\mu_0$ GHz/T and $\mu_0M_0=1025.6\pm0.2$ mT. The linewidth follows the standard linear Gilbert damping model with $\alpha=0.0053$ and $\mu_0\Delta H_i=0.077$ mT. The small values of α and ΔH_i indicate the high quality and homogeneity of sample A-3.

If increasing the power by ten times (plus 10 dBm) the FMR [dotted lines in Fig. 9(b)] shifts to ~-1 mT due to the decreasing M_z by the cone angle of the magnetization precession. Meanwhile, the linewidth of FMR does not show

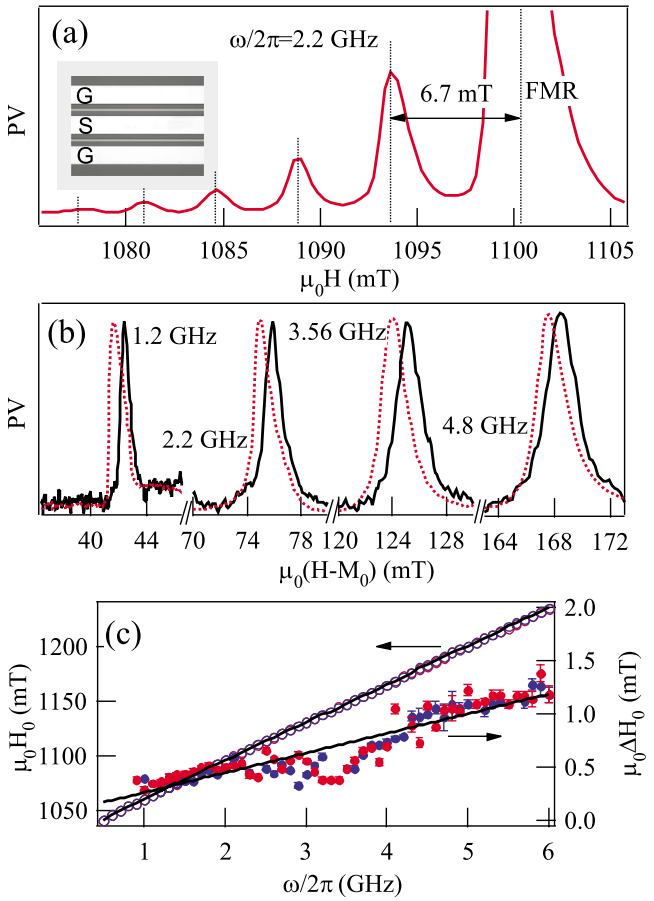

FIG. 9. (Color online) (a) FMR and magnetostatic forward volume modes at 2.2 GHz for sample A-3. (b) FMR for several frequencies at low power excitation with $h=3-5$ μT (black solid lines). The dotted lines are the FMR for ten times higher power compared with solid lines, i.e., $\mu_0 h=9-15$ μT. At both cases h is smaller than h_{th}. (c) Dispersion of FMR (open symbols) and FMR linewidth (solid symbols) at low power excitations. Lines are linear fitting.

any significant change, except for the lowest frequency (1.2 GHz). The significant broadening of the linewidth at 1.2 GHz can be explained by the frequency dependence of the parameter β, which will be discussed in Sec. IV E.

C. FMR response from linear to nonlinear regime

Figures 10(a) and 10(b) show mappings of the FMR PV and PR responses at 2.2 GHz by using lock-in techniques, respectively. Both of them show that there is a critical field h. The shift is proportional to h^2 at $h \ll h_{th}$ and proportional to $h^{2/3}$ at $h \gg h_{th}$. It is well known that the linear FMR shifts according to $H-H_0 \sim -M_0\theta^2/2$ and $\theta \sim h/\Delta H_0$. The fact that the shift becomes slow exactly reflects the unique feature of $\theta \propto h^{1/3}$ in nonlinear magnetization dynamics.

The critical points indicated by arrows in both Figs. 10(a) and 10(b) correspond to an identical value of $\mu_0 h=25$ μT, which is about 50% larger than the Anderson-Suhl threshold $\mu_0 h_{th} \sim 17$ μT calculated by using $\mu_0 \Delta H_0=0.45$ mT measured at a very low power excitation. We find that this is due

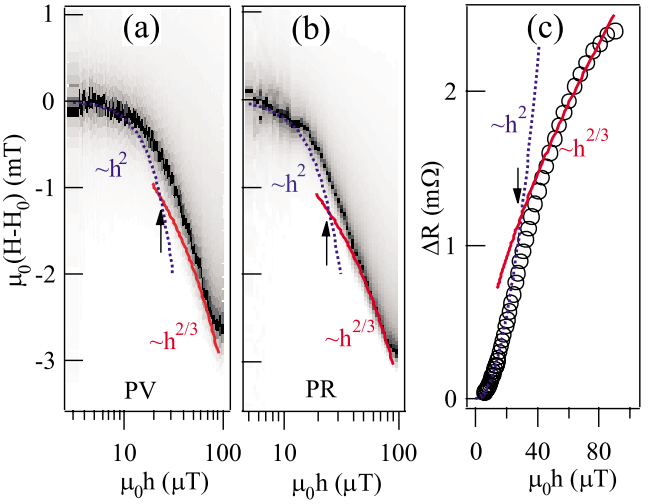

FIG. 10. (Color online) Mappings of FMR (a) PV and (b) PR responses at 2.2 GHz for sample A-3. (c) The resonant amplitude of PR as a function of h at 2.2 GHz. Dotted lines in (a)–(c) represent the linear FMR effect, where the cone angle θ is proportional to h, and solid lines represent a nonlinear FMR shift, where the cone angle is proportional to $h^{1/3}$. Arrows indicate the critical field of the transition from linear to nonlinear FMR.

to the nonzero β. The value of $\beta \sim 0.09$ according to the revised threshold in Eq. (19) agrees well with $\beta=0.1$ deduced from foldover effect discussed in Sec. IV D. The cone angle in this critical point is about 2.3°, as calculated from $\theta=h/(\Delta H_0+\beta M_0\theta^2)$. Due to the contribution of β term, ΔH is broadened to 0.6 mT at h_{th}, which is one third larger than $\mu_0 \Delta H_0=0.45$ mT.

This transition can be further confirmed by the amplitude of the FMR PR response in Fig. 10(c), which is proportional to $\langle m_x^2 \rangle$, i.e., θ^2. Note that the photoresistance ΔR also slows down from an h^2 dependence (dotted lines) to an $h^{2/3}$ dependence (solid line) in Fig. 10(c). The threshold indicated by the arrow in Fig. 10(c) corresponds to $\mu_0 h \sim 29$ μT, which is comparable to the value of $\mu_0 h \sim 25$ μT from both PV and PR mappings. One can further determine $\beta \sim 0.11$ according to Eq. (19).

Depending on the sample structure, the strength of h covers a range of more than four orders of magnitude in our spin dynamos: from a few μT to a few 10 mT. We demonstrate the foldover FMR for three typical samples: A-3, C-10, and C-5 at $\mu_0 h \sim 0.2$, 3 and 30 mT, respectively. As shown in Fig. 11, the foldover FMR under the CW MW excitation shifts from a few mT to about 100 mT with respect to the FMR at low power excitation. We find that the spin-wave resonance also shifts with increased MW power (not shown here). In first-generation samples, such as A-3, the magnetostatic forward volume mode does not cross with FMR because the shift of FMR is less than or comparable to the space between the FMR and magnetostatic forward volume modes. However, magnetostatic modes may be crossing with FMR at high power levels in some second-generation spin dynamos.

As expected, the FMR traces of the up and down sweeps coincide as shown in the inset of Fig. 11(b) when modulating MW amplitude using lock-in techniques. In addition, the

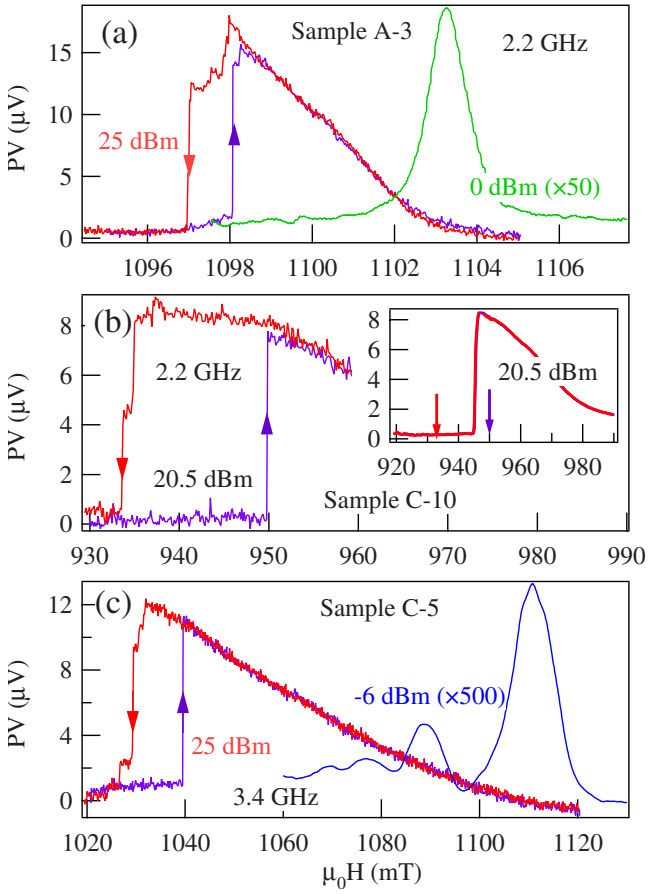

FIG. 11. (Color online) Foldover FMR response for samples (a) A-3, (b) C-10, and (c) C-5 under CW MW excitation. Low power excitation under modulating MW power using lock-in techniques for comparison is also shown in (a) and (c). The inset of (b) demonstrates that traces coincide for both up and down sweeps for a lock-in measurement and the arrows indicate the jump positions in (b).

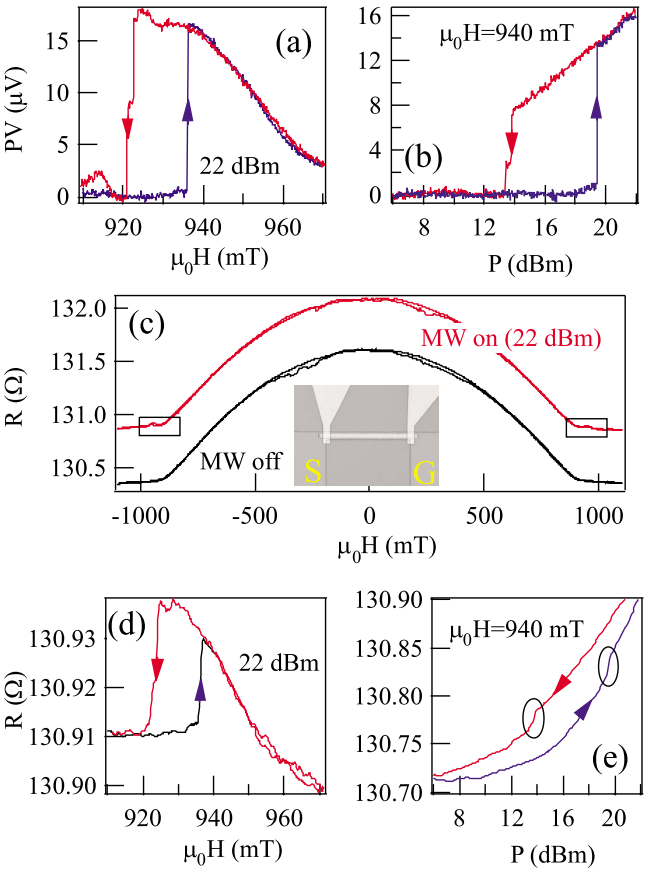

FIG. 12. (Color online) (a) PV and (d) PR foldover responses of sample C-10 by sweeping H field at a fixed microwave power. (b) PV and (e) PR foldover response by sweeping the microwave power at a fixed H field. (c) AMR effect with and without MW illumination. The vicinity of FMR indicated by the square in (c) can be zoomed in as (d). The MW is in the CW mode and the frequency is 2.2 GHz.

jump in PV spectra by the lock-in measurement, which is not as rapid as that under CW MW excitation, is closer to the jump-up, but coincides neither with the jump up nor the jump down in CW MW excitation, even at same MW power level. This is different from the conclusion of Fetisov *et al.*[25] that the pulse data reproduced the up-sweep CW results. It may be caused by the fact that we use an AM rather than a pulse modulation, which may have a different overshoot or ringing behavior of the modulated amplitude.

D. PV foldover FMR response in nonlinear regime

Before quantitatively analyzing foldover effects, we briefly discuss the experimental method to observe the foldover effect. As discussed in Sec. III, a foldover response can be observed by either PV [Fig. 12(a)] or PR [Fig. 12(d)] techniques by sweeping the H field at a fixed MW power. An alternative mean of measurement is sweeping the MW power at a fixed H field, which can be demonstrated by Figs. 12(b) and 12(e). Just as there is a critical h_{th}, there is a critical H in the power-sweep measurement for foldover effect. Foldover FMR by sweeping MW power can only occur at $H < H_{th} \sim H_0 - \sqrt{3}\Delta H$.

The MW heating effect in the nonlinear range can be monitored by the sample resistance. As shown in Fig. 12(c) the resistance of sample C-10 changes by about 0.5 Ω when switching on the MW with an output power of 22 dBm at 2.2 GHz. The dissipated MW energy increases the temperature of the whole chip a few kelvins and $\mu_0 M_0$ decreases a few tenths of a mT, which is at least an order of magnitude smaller than the shift of FMR, a few mT to about 100 mT as shown in Fig. 11. Therefore, the thermal origin of the foldover effect in our samples can be neglected in contrast to that in YIG samples.[26]

The time scale of the heating relaxation is on the order of a few seconds to a few tens of seconds.[30] Therefore, bolometric effects can be effectively suppressed by fast sweeping. The PR foldover effect is shown in Fig. 12(d), where the resistance changes a few 10 mΩ due to the magnetization precession in the nonlinear range. The H field is swept with a speed of 2 mT/s in order to eliminate the bolometric effect. Here, the hysteresis effect confirms the multivalues of the cone angle in the nonlinear range. The cone angle can be roughly estimated to be as large as 12° from θ^2

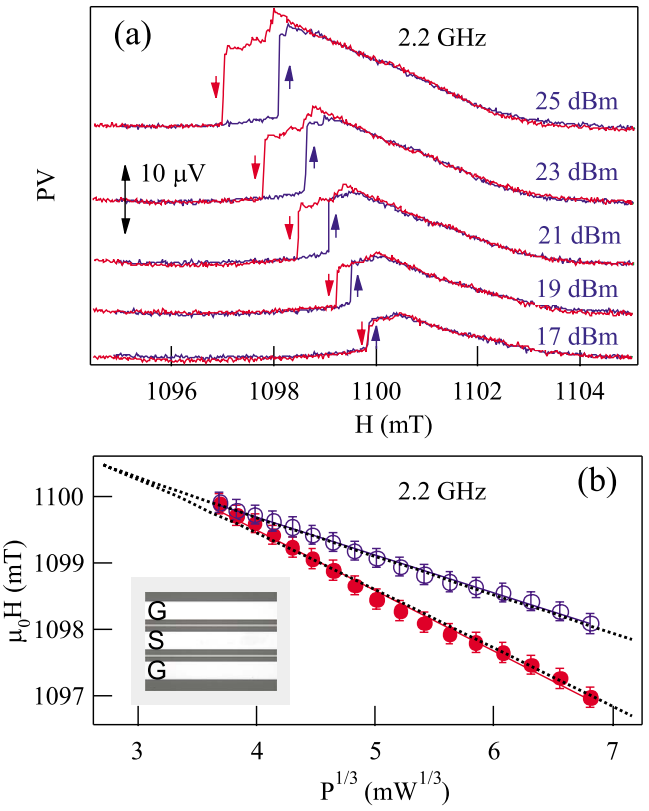

FIG. 13. (Color online) (a) Foldover FMR PV spectra of sample A-3 for several microwave powers at 2.2 GHz. Curves are vertically offset for clarity. (b) H_{up} and H_{down} as functions of $P^{1/3}$ demonstrate a linear dependence at 2.2 GHz (circle symbols), respectively. The dotted lines are calculated via Eq. (15) by using the fitted values of S and β.

$\sim 2\Delta R/\Delta R_{AMR}$, where $\Delta R_{AMR}=1.2\ \Omega$ is the sample resistance change due to AMR effect and $\Delta R=25\ \mathrm{m}\Omega$ is the resistance change due to FMR resonance; the factor of 2 is because only the m_x component contributes to the resistance change in perpendicular magnetization.

The MW photoresistance technique meets a problem when sweeping the MW power. As shown in Fig. 12(e) the PV response was measured by waiting 10 s for every power point with a 0.1 dBm step. Even though it cannot fully relax the MW heating effect and the jumps in the foldover response are smoothed by the bolometric effect.

In principle, there is another way to obtain the foldover FMR response by sweeping the frequency and fixing both P and H as done in Ref. 25. This requires that h remains constant when sweeping ω. However, the coupling parameter S in $h=S\sqrt{P}$ in our spin dynamos is strongly dependent on the frequency (shown in Sec. IV E). It makes it impossible for us to repeat this kind of experiment. We will carefully study the MW power dependence of the foldover effect in three typical samples: A-3 and C-10 in this section and C-5 in the next section, which correspond to different h ranges: a few 0.1 mT, a few mT, and a few 10 mT, respectively. The results confirm the validity of Eq. (2).

Figure 13(a) shows foldover FMR PV spectra for several microwave powers from 25 to 17 dBm at 2.2 GHz for sample A-3. The splitting of up- and down-sweep traces can be distinguished from 17 dBm and the jump appears at a lower power level. Increasing the MW power, both H_{up} and H_{down} shift to low H fields and the splitting increases. As discussed in Sec. II C, H_{up} is not sensitive to ΔH and is linearly proportional to $P^{1/3}$. Therefore, the coupling parameters $S=h/\sqrt{P}$ can be estimated from the slope of H_{up} vs $P^{1/3}$ according to Eq. (13), which shows an excellent agreement with experimental data and the results are $S=0.0087$, 0.0083, and 0.0073 $\mathrm{mT}/\sqrt{\mathrm{mW}}$ for 1.8, 2.0, and 2.2 GHz, respectively.

Interestingly, H_{down} also shows a linear dependence on $P^{1/3}$, which is significantly deviates from the linear P dependence according to the Anderson-Suhl model based on standard linear damping. This exactly demonstrates the effect due to the additional damping term: $\beta M_0\theta^2$. Equation (24) can be used to deduce the value of β for simplest if $\beta \ll 1$, for which the results are $\beta=0.09$, 0.13, and 0.10 for 1.8, 2.0, and 2.2 GHz, respectively. These values are confirmed by the numerical calculation via Eq. (15) [dotted lines in Fig. 13(b)] using the known parameters β and S. The numerical calculation also gives the value of θ_{down}, which is in a range of $3.7°-6.8°$ for $h=50-160\ \mu\mathrm{T}$. The broadening of ΔH due to the β term is 0.4–1.4 mT, which becomes larger than the standard linear damping $\Delta H_0 \sim 0.41-0.45$ at these frequencies.

The h field can be increased one or two orders of magnitudes by using a vertical coupling design, wherein the dominating component of the h vector is h_y. Figure 14 shows similar foldover FMR PV spectra for several microwave powers from 22 to 12 dBm at 2.2 GHz for sample C-10, which has an h as high as a few mT. Parameters $\mu_0 M_0=0.9$ T, $\gamma/2\pi=28.6\mu_0$ GHz/T, $\alpha=0.012$, and $\mu_0\Delta H_i=0.93$ mT are deduced prior from low power lock-in measurements. The extremely large value of ΔH_i compared with that in sample A-3 may be due to the damaged Py surface when sputtering the SiO_2 isolating layer.

The gap between H_{up} and H_{down}, and their shifts with respect to H_0 are all on the order of 10 mT. The coupling parameter were deduced from H_{up} as a function of $P^{1/3}$, which are $S=0.22$ and 0.4 $\mathrm{mT}/\sqrt{\mathrm{mW}}$ for 2.2 and 1.4 GHz, respectively, which is at least an order of magnitude higher than that in sample A-3. The value of h is as high as 5 mT, which is much larger than the value of ΔH_0 (<2 mT). In a traditional picture, the spin may be flipped under such a strong radiation since $\theta \sim 90°$. However, experiments cannot provide any clues for this effect. The result is that the cone angle is not so large because of the broadening ΔH due to the β term.

In sample C-10 H_{down} also shows a linear dependence on $P^{1/3}$, as that in sample A-3. From the slopes the values of β were deduced to be 0.10 and 0.19 for 2.2 and 1.4 GHz, respectively. The foldover effect has also been observed in other frequencies between 1.4 and 2.4 GHz (not shown) and β was found to have a larger value at a lower frequency, which will be confirmed by sample C-5 in a wider frequency range discussed in Sec. IV E. The cone angle is about 17° for both 1.4 and 2.2 GHz at 22 dBm, which is in agreement with the value of 12° estimated from the AMR effect in Figs. 12(c) and 12(d). For precession at this cone angle, the damp-

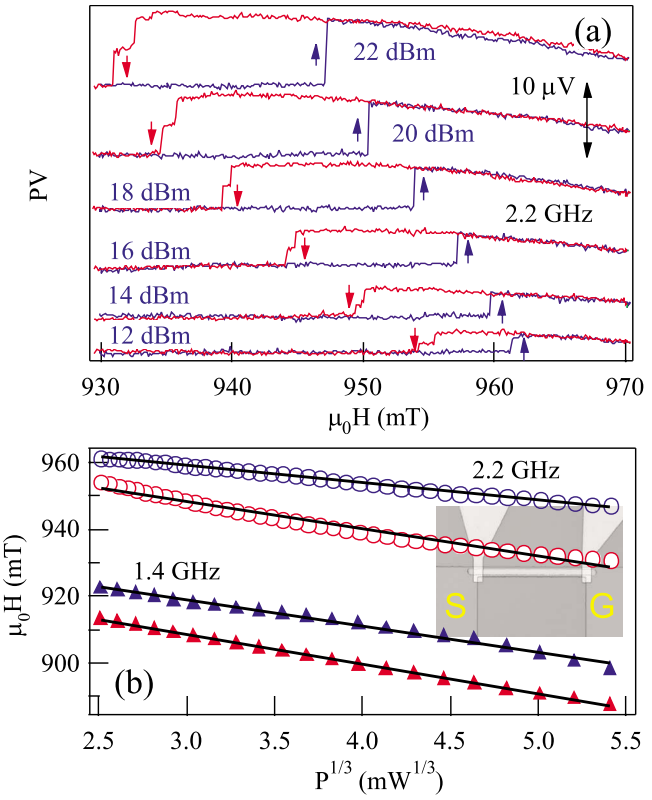

FIG. 14. (Color online) (a) Foldover FMR PV spectra of sample C-10 for several microwave powers at 2.2 GHz. Curves are vertically offset for clarity. (b) H_{up} and H_{down} as functions of $P^{1/3}$ demonstrate a linear dependence at 1.4 GHz (circle symbols) and 2.2 GHz (triangle symbols).

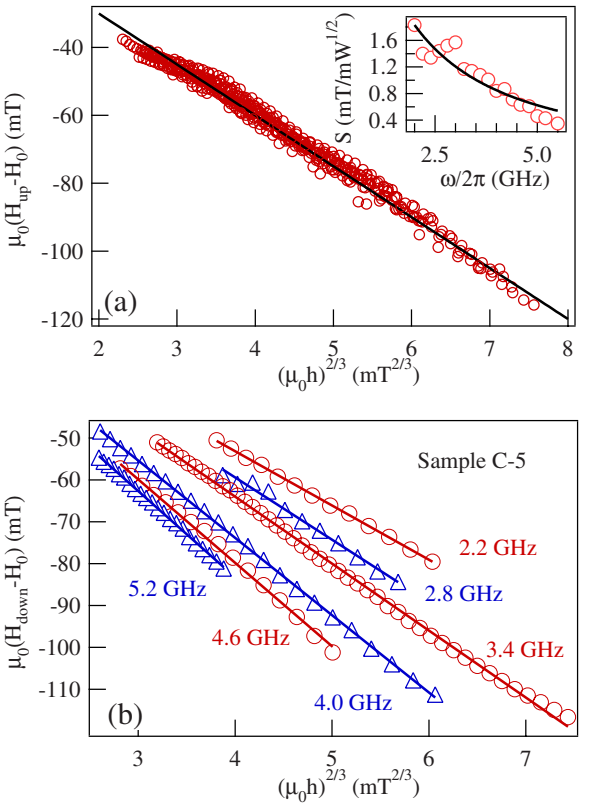

FIG. 15. (Color online) (a) $H_{up}-H_0$ (symbols) of sample C-5 for 18 frequencies between 2.0 and 5.5 GHz are on the same scale guided by the solid line $-3h^{2/3}M_0^{1/3}/2$. The inset shows the frequency dependence of the S parameter. (b) $H_{down}-H_0$ (symbols) of sample C-5 as a function of $h^{2/3}$ for several frequencies demonstrates a linear dependence.

ing is on the order of 10 mT and dominated by β term. Interestingly, $\beta\mu_0 M_0\theta^2=14$ mT at 1.4 GHz is much larger than $\beta\mu_0 M_0\theta^2=8$ mT at 2.2 GHz. This completely reverses the standard linear damping shown in Eq. (1), where ΔH_0 increases with the frequency.

It should be noticed that the jump down always has a mini step with a width between 0.3 and 2.5 mT depending on both the frequency and the MW power. At this moment we do not know the origin of such a mini step. Nevertheless, the existence of such a mini step does not affect the value of β since its width is one order of magnitude smaller than H_0-H_{down}.

E. Frequency dependence of parameter β

As discussed in Sec. IV D, the parameter β is strongly dependent on the frequency. Moreover, Eq. (1) is completely reversed by the β term up to a certain cone angle. In order to confirm and carefully study these effects, sample C-5 was fabricated with a broadband of frequency with $\mu_0 h$ as high as 10 mT, and $\mu_0 M_0=1$ T, $\gamma/2\pi=29.2\mu_0$ GHz/T, $\alpha=0.009$ and $\mu_0\Delta H_i=0.88$ mT.

The power-dependent Foldover effect has been observed from 2.2 to 5.5 GHz. The S parameter was deduced from H_{up}. As shown in the inset of Fig. 15(a), the frequency dependence of S can be well described by the energy loss in a transmission line according to $\ln S \propto -\alpha_t\sqrt{\omega}$, where α_t is the attenuation constant of the structure.[36] The plot of $H_{up}-H_0$ as a function of $h^{2/3}$ is shown in Fig. 15(a). The experimental data for all frequencies are on the same scale, which can be guided by the solid line $H_{up}-H_0=-3h^{2/3}M_0^{1/3}/2$.

We can also plot $H_{down}-H_0$ as a function of $h^{2/3}$ as in Fig. 15(b). Obviously, it has a linear dependence for all frequencies. Another feature is that its slope is larger at higher frequencies, which is indicated by the larger shift at a fixed h. It is well known that the shift of FMR is due to the decrease in $M_z=(1-\theta^2/2)M_0$ at high power levels, where the cone angle $\theta\sim h/\Delta H$. The conclusion that ΔH is smaller at higher frequencies is in contradiction to Eq. (1).

The nonlinear damping parameter β can be quantitatively deduced from H_{down} according to Eq. (21) for 2.2–5.5 GHz. It is found that the frequency dependence of β can be well fitted to an empirical relation $\beta=4.0/\omega$, where ω is in units of GHz. This indicates that there is a cutoff frequency of $\omega/2\pi=2\sqrt{3}\times 4.0/2\pi\sim 2.2$ GHz for foldover effect. Indeed, the foldover effect disappears when $\omega<2.2$ GHz even though the FMR shift can been found to be as large as $\sim$100 mT at high power levels. Because of the attenuation of MW, both PV and h become weaker at higher frequencies. There are no enough power points for the foldover effect to deduce a precise value of β when $\omega>5.5$ GHz.

ΔH can be calculated according to Eq. (2) by using the known parameters ΔH_i, α, and β. An interesting feature is

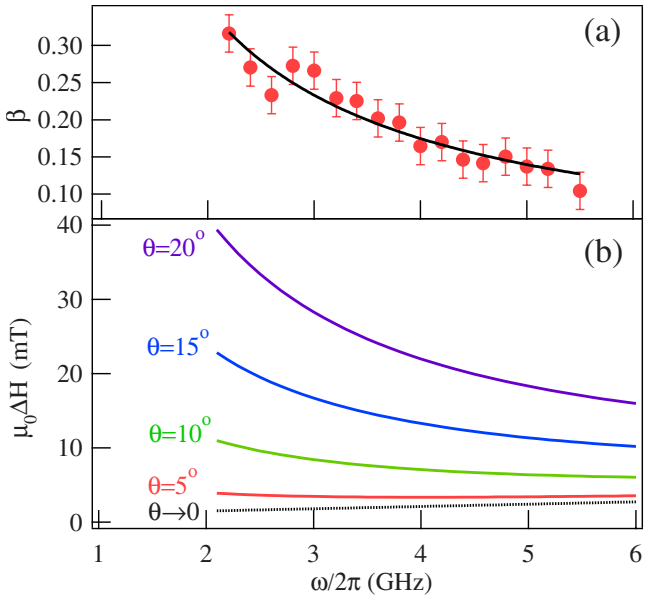

FIG. 16. (Color online) (a) The measured frequency dependence of the nonlinear damping parameter β (symbols) and the empirical relation of $\beta=4.0/\omega$ (solid line). (b) ΔH including both the standard linear Gilbert damping and β terms as a function of frequency for several cone angles. The dotted line is for standard linear Gilbert damping.

that Eq. (1) is valid only in a low power range. Once the cone angle is on the order a few degrees, the linewidth is dominated by β term as shown in Fig. 16(b).

V. CONCLUSIONS

We have presented a systematic investigation of linear and nonlinear FMRs, which covers a wide field $\mu_0 h$ range from a few μT to a few 10 mT. We demonstrate the inadequacy of Eq. (1) for nonlinear FMR. The nonlinear damping β term in Eq. (2), which has been neglected in a conventional theory, must be taken into account to explain the unique feature of nonlinear FMR.

We have compared the similarity of mathematics for a pendulum and FMR. In some sense, the precession of the magnetization can be simplified by using the concept of cone angle. A theoretical model of FMR based on the nonlinear oscillator is therefore developed by introducing a nonlinear damping term: $\beta M_0 \theta^2$. This model can quantitatively describe the foldover effect in Py microstrips. From the revised h_{th} and the empirical frequency dependence of β, we find a phase diagram for the foldover effect. It may explain why the foldover effect was not observed in any ferromagnetic metal previously, even though Anderson and Suhl predicted it half a century ago.

We would like to discuss the possible origin of the β term. The Gilbert damping term in the LLG equation only indicates the existence of a friction force; however, it does not deal with the origin of this friction force. It is believed that dissipative mechanisms of the dynamic magnetization can be roughly attributed to direct relaxation to the lattice or conduction electrons and to indirect relaxation via excitation of many magnetic modes before the spin angular momentum is ultimately dissipated to the lattice. Here, the direct relaxation via magnetostriction to the lattice is not important since the magnetostriction is very low in Py. The direct relaxation via conduction electrons is believed to be due to spin-orbit interactions accompanied by interband and intraband scattering,[37] which result in a frequency-independent damping constant α. At high power levels, the indirect relaxation becomes dominant, which can be also demonstrated by our experimental results. Suhl[9] carefully discussed the possibility of nonlinear spin-wave generation and indicated that there are two main channels to transfer the spin angular momentum at high power levels: first-order Suhl spin-wave instability via $\omega_k = \omega/2$ and second-order Suhl spin-wave instability via $\omega_k = \omega$, where ω_k is the frequency of spin wave. Very recently, Dobin and Vicota[8,38] developed an analytical theory related to Suhl's spin-wave instability[9] and studied the spin angular momentum transfer from the uniform ($k=0$) procession mode to the nonuniform ($k \neq 0$) procession mode. They found that three-magnon (in bulk) and four-magnon (in thin films) scattering processes are responsible for rapid relaxation. In principle, the generation of spin wave is different from standard Gilbert damping since standard Gilbert damping dissipates the energy to heat while energy only redistributes for Suhl's spin wave. However, both of them align the magnetization to the external applied H direction. Therefore, the generation of Suhl's spin wave may be regarded as an additional damping term in a phenomenological framework. Indeed, Back *et al.*[39] observed an effective increase in damping for large magnetization precession in cobalt films under a pulsed magnetic field. Dobin and Vitora[8] found that the four-magnon process with an intrinsic Gilbert damping constant $\alpha=0.005$ gives a very similar pattern to $\alpha=0.037$ without four-magnon scattering when they tried to simulate experimental results of Back *et al.*[39] Stöhr and Siegmann agreed with the significant contribution of Suhl's spin-wave instability to the dissipation; however, they indicated that the simulation fell short by a factor of 2 to fully account for the observed damping.[40]

Another main feature of Suhl's spin-wave instability is its thickness dependence. The phase space for Suhl degenerated spin waves decreases with the film thickness for an in-plane static field. This effect has been observed by Patton *et al.* as early as 1967 (Ref. 41) that the linewidth of FMR increases linearly with the film thickness. In the case of a thin film magnetized normally to its surface, it is generally believed that the possibility of degenerate spin-wave modes and parametric spin-wave processes can be eliminated because the uniform precession mode falls at the bottom of the spin-wave band.[25,42] However, with an open cone angle the uniform precession mode and the nonuniform precession mode couple together and may degenerate. Experimentally, we observe that the FMR and the magnetostatic forward volume mode are indeed crossed with an increasing MW power. It is therefore interesting to study the spin-wave band by taking its power dependence into account.

While the exact microscopic origin of the β term remains to be sought out theoretically, in this paper we demonstrate a method that can precisely determine the linewidth and provide a quantitative form of the linewidth. This knowledge

may help people to understand the unknown relaxation mechanisms, which must be active at large precession angles as pointed out by Stöhr and Siegmann.[40] This is also technologically important for magnetic data storage, which is expected to change the magnetization direction over very large angles.

ACKNOWLEDGMENTS

The authors acknowledge N. Mecking, E. Himbeault, X. L. Fan, L. H. Bai, and H. Xiong for useful discussions. This work was funded by NSERC and URGP (C.-M.H.).

[1] S. Sun, C. B. Murray, D. Weller, L. Folks, and A. Moser, Science **287**, 1989 (2000).
[2] C. Thirion, W. Wernsdorfer, and D. Mailly, Nature Mater. **2**, 524 (2003).
[3] Y. Nozaki, K. Tateishi, S. Taharazako, M. Ohta, S. Yoshimura, and K. Matsuyama, Appl. Phys. Lett. **91**, 082510 (2007).
[4] J. Podbielski, D. Heitmann, and D. Grundler, Phys. Rev. Lett. **99**, 207202 (2007).
[5] G. Woltersdorf and C. H. Back, Phys. Rev. Lett. **99**, 227207 (2007).
[6] X. L. Fan, Y. S. Gui, A. Wirthmann, G. Williams, D. S. Xue, and C.-M. Hu, Appl. Phys. Lett. **95**, 062511 (2009).
[7] T. L. Gilbert, IEEE Trans. Magn. **40**, 3443 (2004).
[8] A. Yu. Dobin and R. H. Victora, Phys. Rev. Lett. **90**, 167203 (2003).
[9] H. Suhl, J. Phys. Chem. Solids **1**, 209 (1957).
[10] V. Tiberkevich and A. Slavin, Phys. Rev. B **75**, 014440 (2007).
[11] L. D. Landau and E. M. Lifshitz, *Mechanics*, 2nd ed. (Pergamon Press, Oxford, 1969).
[12] P. W. Anderson and H. Suhl, Phys. Rev. **100**, 1788 (1955).
[13] M. T. Weiss, Phys. Rev. Lett. **1**, 239 (1958).
[14] H. Suhl, J. Appl. Phys. **31**, 935 (1960).
[15] P. Gottlieb, J. Appl. Phys. **31**, 2059 (1960).
[16] J. I. Masters, J. Appl. Phys. **31**, S41 (1960).
[17] I. B. Goldberg, J. Appl. Phys. **51**, 1857 (1980).
[18] L. M. Silber, C. E. Patton, and H. F. Naqvi, J. Appl. Phys. **54**, 4071 (1983).
[19] K. D. McKinstry, C. E. Patton, and M. Kogekar, J. Appl. Phys. **58**, 925 (1985).
[20] D. J. Seagle, S. H. Charap, and J. O. Artman, J. Appl. Phys. **57**, 3706 (1985).
[21] Y. T. Zhang, C. E. Patton, and M. V. Kogekar, IEEE Trans. Magn. **22**, 993 (1986).
[22] K. Gnatzig, H. Dötsch, and A. Brockmeyer, J. Appl. Phys. **62**, 4839 (1987).
[23] Y. T. Zhang, C. E. Patton, and G. Srinivasan, J. Appl. Phys. **63**, 5433 (1988).
[24] M. Chen, C. E. Patton, G. Srinivasan, and Y. T. Yang, IEEE Trans. Magn. **25**, 3485 (1989).
[25] Y. K. Fetisov, C. E. Patton, and V. T. Synogach, IEEE Trans. Magn. **35**, 4511 (1999).
[26] Y. K. Fetisov and C. E. Patton, IEEE Trans. Magn. **40**, 473 (2004).
[27] Y. S. Gui, N. Mecking, X. Zhou, Gwyn Williams, and C.-M. Hu, Phys. Rev. Lett. **98**, 107602 (2007).
[28] Y. S. Gui, N. Mecking, and C.-M. Hu, Phys. Rev. Lett. **98**, 217603 (2007).
[29] N. Mecking, Y. S. Gui, and C.-M. Hu, Phys. Rev. B **76**, 224430 (2007).
[30] Y. S. Gui, N. Mecking, A. Wirthmann, L. H. Bai, and C.-M. Hu, Appl. Phys. Lett. **91**, 082503 (2007).
[31] Y. S. Gui, A. Wirthmann, N. Mecking, and C.-M. Hu, Phys. Rev. B **80**, 060402(R) (2009).
[32] N. Minorsky, *Nonlinear Oscillations* (D. Van Nostrand Company, Inc., Princeton, NJ, 1962).
[33] M. N. Bogoliubov and Y. A. Mitropolsky, *Asymptotic Methods in the Theory of Non-linear Oscillations* (Hindustan Publishing Corporation, Delhi, India, 1961).
[34] S. T. Thornton and J. B. Marion, *Classical Dynamics of Particles and Systems*, 5th ed. (Thomson Brooks/Cole, Australia, 2004).
[35] L. H. Bai, Y. S. Gui, A. Wirthmann, E. Recksiedler, N. Mecking, C.-M. Hu, Z. H. Chen, and S. C. Shen, Appl. Phys. Lett. **92**, 032504 (2008).
[36] B. S. Guru and H. R. Hiziroğlu, *Electromagnetic Field Theory Fundamentals*, 2nd ed. (Cambridge University Press, Cambridge, England, 2004).
[37] B. Heinrich, J. F. Cochran, and R. Hasegawa, J. Appl. Phys. **57**, 3690 (1985).
[38] A. Yu. Dobin and R. H. Victora, J. Appl. Phys. **95**, 7139 (2004).
[39] C. H. Back, R. Allenspach, W. Weber, S. S. P. Parkin, D. Weller, E. L. Garwin, and H. C. Siegmann, Science **285**, 864 (1999).
[40] J. Stöhr and H. C. Siegmann, *Magnetism From Fundamentals to Nanoscale Dynamics* (Springer, Berlin, 2006), pp. 727–733.
[41] C. E. Patton, C. H. Wilts, and F. B. Humphrey, J. Appl. Phys. **38**, 1358 (1967); C. E. Patton, *ibid.* **39**, 3060 (1968).
[42] R. D. McMichael and P. E. Wigen, Phys. Rev. Lett. **64**, 64 (1990).